IOP Publishing Nanotechnology

Nanotechnology 27 (2016) 055703 (7pp) doi:10.1088/0957-4484/27/5/055703

Thermal transport properties of MoS_2 and $MoSe_2$ monolayers

Ali Kandemir[1], Haluk Yapicioglu[2], Alper Kinaci[3], Tahir Çağın[4] and Cem Sevik[5]

[1] Department of Materials Science and Engineering, Faculty of Engineering, Anadolu University, Eskisehir, TR 26555, Turkey and Department of Materials Science and Engineering, İzmir Institute of Technology, İzmir, TR 35430, Turkey
[2] Department of Industrial Engineering, Faculty of Engineering, Anadolu University, Eskisehir, TR 26555, Turkey
[3] Center for Nanoscale Materials, Argonne National Laboratory, Lemont, IL 60439 USA
[4] Artie McFerrin Department of Chemical Engineering and Material Science and Engineering, Texas A and M University, College Station, TX 77845–3122, USA
[5] Department of Mechanical Engineering, Faculty of Engineering, Anadolu University, Eskisehir, TR 26555, Turkey

E-mail: csevik@anadolu.edu.tr

Received 5 November 2015
Accepted for publication 9 December 2015
Published 11 January 2016

Abstract

The isolation of single- to few-layer transition metal dichalcogenides opens new directions in the application of two-dimensional materials to nanoelectronics. The characterization of thermal transport in these new low-dimensional materials is needed for their efficient implementation, either for general overheating issues or specific applications in thermoelectric devices. In this study, the lattice thermal conductivities of single-layer MoS_2 and $MoSe_2$ are evaluated using classical molecular dynamics methods. The interactions between atoms are defined by Stillinger–Weber-type empirical potentials that are developed to represent the structural, mechanical, and vibrational properties of the given materials. In the parameterization of the potentials, a stochastic optimization algorithm, namely particle swarm optimization, is utilized. The final parameter sets produce quite consistent results with density functional theory in terms of lattice parameters, bond distances, elastic constants, and vibrational properties of both single-layer MoS_2 and $MoSe_2$. The predicted thermal properties of both materials are in very good agreement with earlier first-principles calculations. The discrepancies between the calculations and experimental measurements are most probably caused by the pristine nature of the structures in our simulations.

S Online supplementary data available from stacks.iop.org/nano/27/055703/mmedia

Keywords: transition metal dichalcogenides, thermal conductivity, molecular dynamics, Green–Kubo

(Some figures may appear in colour only in the online journal)

1. Introduction

Recently, a new class of two-dimensional layered materials, transition metal dichalcogenides (TMDs), have stimulated an intense research effort, mainly due to their unique electronic and magnetic properties compared to the zero-band-gap semiconductor graphene and insulator hexagonal boron nitride (white graphene). Numerous first-principles studies have revealed that semiconductor TMDs, MX_2 (where M = Cr, Mo and W and X = S, Se, Te), with band gap values ranging from visible to near infrared, may offer solutions for nanoelectronic and optoelectronic applications where graphene and hexagonal boron nitride are inadequate. Moreover, single-layer and few-layer MoS_2 [1, 2], $MoSe_2$ [3], $MoTe_2$ [3], WS_2 [4, 5], and

WSe_2 [6, 7], and also heterostructures [8, 9] composed of these materials, have already been fabricated and investigated as ideal candidates for a variety of practical technological applications including catalysis [10], energy storage [11], sensing [12], and electronic devices such as field-effect transistors [7, 13, 14] and logic circuits [12, 15]. One of the key parameters of design in these devices is the thermal conductivity of the constituents since in many cases small electronic parts produce excess heat. As two-dimensional TMDs are being considered as parts of these assemblies, the characterization of their thermal transport properties is critical.

A specific application of low-dimensional TMDs that requires strict thermal control is thermoelectrics [16–19], i.e. energy harvesting and cooling devices. Recently, there have been reports of low lattice thermal conductivity for MoS_2 and WS_2 and a high power factor for MoS_2. In these preliminary works, the experimentally measured value of lattice thermal conductivity of few-layer MoS_2 has been reported to be below 55.0 $Wm^{-1}K^{-1}$ [20–22], and those of single- and double-layer WS_2 have been reported as 32.0 $Wm^{-1}K^{-1}$ and 53.0 $Wm^{-1}K^{-1}$ [23], respectively. These room-temperature values, around two orders smaller than the lattice thermal conductivity of single-layer graphene, have been reproduced by classical molecular dynamics (MD) and first-principles calculations [24–31] as well. Additionally, the promising thermoelectric performance of these materials has been reported. The maximum dimensionless figure of merit (*ZT*) of single-layer MoS_2 has been calculated to be around 0.6 by Huang *et al* [18]. In addition, for *n*-type doped bilayer MoS_2, $MoSe_2$, and WSe_2, the peak value of *ZT* has been calculated to be as much as 1.6, 2.39, and 2.1, respectively [17, 18, 32]. These reported values clearly indicate the possibility of using two-dimensional TMDs for thermoelectric applications, and the necessity of fundamental and comparative studies on the lattice thermal transport properties of these monolayer materials due to the direct relation between thermal conductivity and thermoelectric performance figure of merit, *ZT*.

The systematic characterization of lattice thermal transport in single-layer TMDs is far from complete. A relatively fast and reliable method to investigate lattice thermal conductivity is to use empirical potentials that describe the atomic vibrations well. In this respect, as a first step, we focus on two of these structures, namely MoS_2 and $MoSe_2$, and develop Stillinger–Weber (SW)-type [33] interaction potential parameter (IPP) sets with particular attention on reproducing structural, mechanical, and vibrational properties. By utilizing the IPPs and MD simulations, we further calculate the thermal transport properties of single-layer MoS_2 and $MoSe_2$ crystals.

2. Computational details

The form of SW interatomic potential parameters [33] used in this study can be written as,

$$E = \sum_i \sum_{j>i} \phi_2(r_{ij}) + \sum_i \sum_{j\neq i k>j} \sum \phi_3(r_{ij}, r_{ik}, \theta_{ijk}), \quad (1)$$

$$\phi_2(r_{ij}) = A_{ij}\left(\frac{B_{ij}}{r_{ij}^4} - 1\right)\exp\left[\frac{\rho_{ij}}{r_{ij} - r_{ij}^{\max}}\right], \quad (2)$$

$$\phi_3(r_{ij}, r_{ik}, \theta_{ijk}) = K_{ijk}\exp\left[\frac{\rho_{ij}}{r_{ij} - r_{ij}^{\max}} + \frac{\rho_{ik}}{r_{ik} - r_{ik}^{\max}}\right] \times (\cos\theta_{ijk} - \cos\theta_{0,ijk})^2 \quad (3)$$

where ϕ_2 and ϕ_3 define the bond stretch (two-body) and bond bending (three-body) interactions, respectively. The summation indices *j* and *k* are the neighbors of atom *i* within a radius of $r^{\max}$ in equations (2) and (3). The terms r_{ij} and r_{ik} indicate the pair separations and θ_{ijk} is the angle between the separation vectors centering on atom *i*.

In describing single-layer MoX_2 (X = S, Se) structures, we consider three stretching terms, namely Mo–Mo, Mo–X, and X–X within the SW formalism. For angle bending, in contrast to stretching, we distinguish the chalcogens with subscripts 'u' and 'd' indicating whether these atoms are above or below the molybdenum layer, as seen on figure 1. This distinction is needed to correctly represent the asymmetric chalcogen polyhedra around molybdenum. We defined three three-body terms: $X_{u,(d)}$–Mo–$X_{u,(d)}$, Mo–$X_{u,(d)}$–Mo and X_u–Mo–X_d. The first term represents the angle between two chalcogens (both above or both below the Mo-plane) and Mo which is at the center. The second term is the angle between two Mo and a chalcogen (above or below the Mo-plane) which is at the center. The third term is the angle between two chalcogens (one above and one below the Mo-plane) and Mo at the center. These angles are shown as θ_1, θ_2, and θ_3, respectively, in figure 1.

Using global optimization schemes to obtain force-field parameter sets is becoming increasingly accepted in the community [34, 35]. There are various approaches and algorithms for global optimization, such as particle swarm optimization (PSO), genetic algorithms, simulated annealing, basin hopping, etc. These methods are very advantageous because one can sample much greater volumes in the parameter space and no intuitive initial guesses are needed. In this study, the SW parameters are generated by using a PSO algorithm which is a population-based stochastic optimization method developed by Kennedy and Eberhart [36]. It is inspired by the social behavior of bird flocking and/or fish schooling. Throughout the optimization procedure, each particle represents a candidate solution to the problem at hand and particles keep a record of the best solution they experience and share this information with the particles in their neighborhood. There are various neighborhood definitions for PSO in the literature [37]. The neighborhood definition employed in this study is the fully connected topology, in which each particle can communicate with the whole swarm. In PSO, each particle is composed of three vectors (current location, **c**, current velocity, **v**, and the best solution found by the particle, **p**) and two fitness values (*c*-fitness and *p*-fitness, which represent the particle's current value and the best value of the objective function, respectively). The dimensions of the **p**, **c**, and **v** vectors correspond to the number of decision variables. The values stored in the **p** and **c** vectors are the

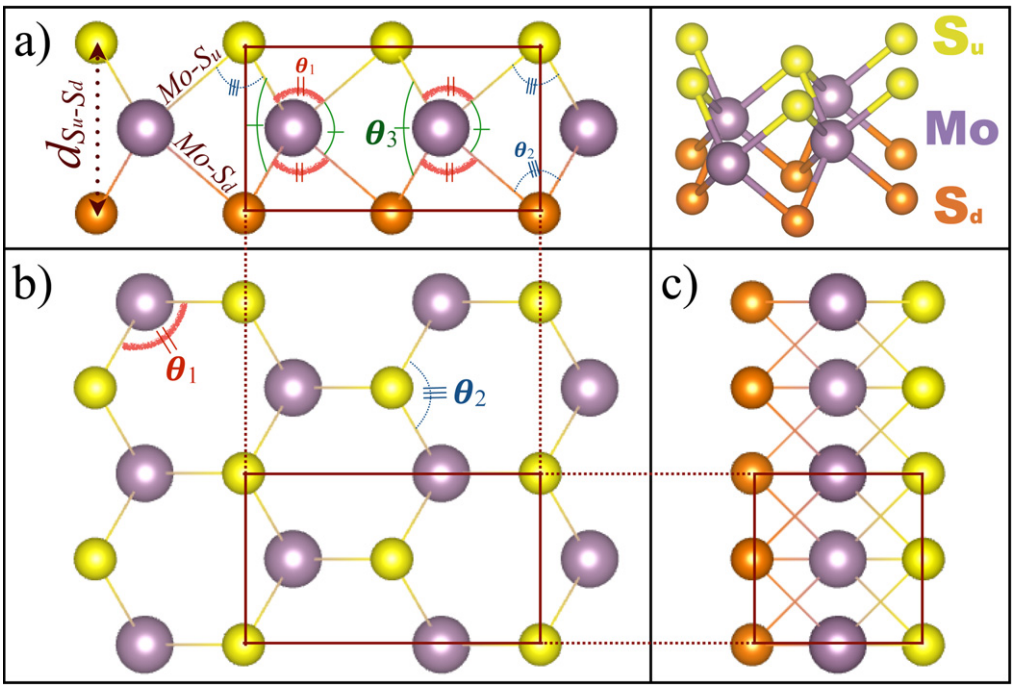

Figure 1. Schematic representations of the single-layer MoS_2 structure from different angles. S_u and S_d represent sulfide atoms that are above and below the molybdenum layer. Mo–S_u and Mo–S_d show bond stretching terms between molybdenum and the two distinct sulfurs. θ_1, θ_2, and θ_3 correspond to three-body interactions: S_u–Mo–S_u (equivalently S_d–Mo–S_d), Mo–S_u–Mo (equivalently Mo–S_d–Mo), and S_u–Mo–S_d, respectively. $d_{S_u-S_d}$ is the closest distance between S_u and S_d. A separate plot for $MoSe_2$ is not provided since it is isostructural to MoS_2.

values of the decision variables, whereas the values stored in **v** are the amount of perturbation to be used in the next iteration of the search. At every iteration t, the velocity and the current position of particle i are updated according to the formulae

$$v_{id}^{t} = K\,[v_{id}^{t-1} + \varphi_1 \mathrm{U}(0,\,1)(p_{id}^{t-1} - c_{id}^{t-1}) + \varphi_2 \mathrm{U}(0,\,1)(p_{gd}^{t-1} - c_{id}^{t-1})], \tag{4}$$

$$c_{id}^{t} = c_{id}^{t-1} + v_{id}^{t} \tag{5}$$

where $\mathbf{c}_i$ is the current position of particle i, $\mathbf{v}_i$ is the current velocity of particle i, $\mathbf{p}_i$ is the best solution identified by particle i, $\mathbf{p}_g$ is the best solution in the neighborhood of particle i. φ_1, and φ_2 are learning rates governing the cognition and social interaction within the swarm, respectively. d is the dth dimension of the corresponding vector, $d = 1, 2, ..., D$ (number of decision variables), and U(0, 1) is a uniform random number in the interval [0, 1]. K is defined as the constriction coefficient which aims at preventing explosion during velocity update as explained in [38]. At every iteration, the best particle of the swarm is first identified by comparing the p-fitness values of the particles and the same particle (indexed by g) is used to update the velocity vectors of the whole swarm. Once **c** is updated c-fitness is computed and compared against p-fitness. If c-fitness is better than p-fitness, **p** is replaced by **c**.

In the current implementation, the dimension of the particles (i.e. the dimensions of **p**, **c**, and **v**) is determined by the number of parameters used to 'optimize' the fitness function (lattice constant, bond angles, bond lengths, elastic constants, and phonon frequencies). Since there are several crystal characteristics that need to be optimized simultaneously, the fitness function is defined as the normalized summation of desired crystal characteristics. To be more precise,

$$c - \text{fitness} = \sum_{j=1}^{N}\left(\frac{|\mathrm{dc}_j - \mathrm{ac}_j|}{\mathrm{dc}_j}\right) \tag{6}$$

where dc_j denotes the desired value of characteristic j (obtained by first-principles calculations), ac_j denotes the actual value obtained through empirical potential for the instantaneous set of parameters, and N is the number of characteristics to be optimized simultaneously. During the optimization process the SW parameter sets are passed to the GULP [39] code with which the properties of MoS_2 and $MoSe_2$ are calculated. After every update of particles according to (4) and (5), a call to GULP is made to obtain the vector of actual characteristics, and these values are used to compute the fitness of the current particle according to (6). The pseudocode of the PSO algorithm as used in this study is given in the supplementary data, section 1 available at stacks.iop.org/nano/27/055703/mmedia.

The desired value database used in the PSO procedure is generated by first-principles calculations based on density functional theory (DFT) [40] as implemented in the Vienna *ab initio* simulation package [41–43]. In these simulations, the projector augmented wave pseudopotentials [44, 45] from the standard distribution are incorporated to describe the core–valence interaction. For the electron exchange-correlation, the generalized gradient approximation within the

Perdew–Burke–Ernzerhof formulation is used. For both structures, a plane wave cut-off energy of 500 eV is used. The Brillouin zone of the primitive cell is sampled by a Γ point centered 26 × 26 × 1 *k*-point mesh within the Monkhorst–Pack scheme. The phonon calculations are performed on 4 × 4 × 1 super-cell structures with a Γ point centered 8 × 8 × 1 *k*-point mesh for the Brillouin zone sampling. A 20 Å vacuum spacing is used to separate the adjoint monolayers along the *z*-direction to avoid spurious interaction between the periodic images.

The thermal conductivity of each material is investigated through MD simulations. These calculations are performed using LAMMPS [46, 47]. The existing SW form in this code is different from the one fitted with PSO, thus an appropriate form is implemented for MD simulations. The new SW-type interatomic potential module is tested against the GULP results and no discrepancy is detected. Further information including vibrational properties calculated with both codes, parameter tables, the nature of code modifications, and the parameter conversion scheme between the codes can be found in in the supplementary data, sections 2–5 available at stacks.iop.org/nano/27/055703/mmedia. The thermal conductivity of single-layer MoS_2 and $MoSe_2$ calculated using the Green–Kubo relations derived from the fluctuation dissipation theorem [48, 49] and equivalently by an expression akin to the Einstein diffusion relationships [50, 51] is as follows,

$$\kappa_{\mu\mu} = \frac{1}{Vk_BT^2}\lim_{t\to\infty}\frac{1}{2t}\langle[R_\mu(t) - R_\mu(0)]^2\rangle \quad (7)$$

where T, V, and k_B are the temperature, volume, and Boltzmann constant, respectively, and R_μ is the time integration of heat current in direction μ. Ordinarily, R_μ for a single particle is the total energy of the particle ϵ_i times its unwrapped coordinate $r_{i\mu}$ in the simulation domain. The total R_μ of the system is calculated by a summation over all particles as follows,

$$R_\mu = \sum_i r_{i\mu}\epsilon_i, \quad (8)$$

which can be thought of as an energy moment vector for the system [52].

The reported values are calculated by averaging the results of eight distinct MD simulations, which were started with different initial particle velocities. The size of the considered periodic two-dimensional simulation cell for each structure is ∼20 nm ×∼20 nm (which we obtain from the converged thermal conductivity at 500 K, roughly 13000 atoms). Cross-sectional areas of the considered structures are predicted using the mean van der Waals distance for hexagonal bulk crystals as the height (0.615 and 0.650 nm for MoS_2 and $MoSe_2$, respectively). For only $MoSe_2$, a constant neighbor list is applied due to the hard cut-off of the SW potential. Before the data are collected for thermal conductivity calculations, the systems are relaxed for 500 ps. The systems are allowed to evolve for a minimum of 5 ns with a time step of 0.5 fs in a microcanonical ensemble for data collection. Previously, we showed that this simulation length is appropriate for graphene and hexagonal boron nitride [53–55] both of which have higher thermal conductivities and thus longer heat current autocorrelation tails than the studied TMDs.

Table 1. The lattice parameter (a_0), the distance between two chalcogen atoms above and below the Mo layer (d_{X_u,X_d}), elastic constants (C_{11} and C_{12}), Young's modulus (Y), and Poisson's ratio (ν) of MoS_2 and $MoSe_2$ evaluated with both DFT and the developed IPP set.

	a_0 (Å)	$d_{X_u-X_d}$ (Å)	C_{11} (N m^{-1})	C_{12} (N m^{-1})	Y (N m^{-1})	ν
MoS_2						
DFT	3.18	1.56	132.7	33.0	124.5	0.25
SW	3.20	1.63	133.0	39.4	121.4	0.30
$MoSe_2$						
DFT	3.32	1.67	106.9	25.6	100.8	0.24
SW	3.32	1.66	114.1	43.3	97.6	0.38

3. Results

The training set for the IPP set to represent single-layer MoS_2 and $MoSe_2$ includes lattice parameters (a_0); the distance between two chalcogen atoms, one above and one below the Mo layer (d_{X_u,X_d}); elastic constants (C_{11} and C_{12}), Young's moduli (Y), and Poisson's ratios (ν). In table 1, we present the results of DFT calculations regarding these properties of both materials.

To capture correct lattice thermal transport behavior we also considered phonon frequencies in the training set. Again DFT calculations are performed to generate phonon dispersions in the first Brillouin zone. In figures 2(a) and (b), we present phonon dispersions along high-symmetry reciprocal space directions for MoS_2 and $MoSe_2$. In the acoustic regime, the dispersion in both materials is similar except that MoS_2 has higher mode frequencies compared to $MoSe_2$. This in line with the prediction of larger elastic constants and Young's modulus for MoS_2. Considering fundamental kinetic theory, thermal conductivity is related to phonon group velocities, relaxation times and heat capacity (i.e. mode populations). With significantly higher frequencies it can be expected that MoS_2 has higher group velocities even though $MoSe_2$ has a slightly smaller Brillouin zone. Furthermore the acoustic–optical phonon gap is smaller in $MoSe_2$ which can lead to increased scattering and a decreased relaxation time for acoustic modes (the annihilation process of two acoustic phonon modes into one optical mode, $\omega_A + \omega'_A = \omega''_O$, is suppressed because of the energy conservation requirement [26]). In both materials, the dispersion in optical modes is limited so the optical phonon contribution to lattice thermal conduction is lower compared to acoustic modes.

We used the first-principles based properties and vibrational frequencies and PSO algorithm to train our SW-type force field. In tables 2 and 3 we present the two-body and the three-body parameters obtained at the end of the training

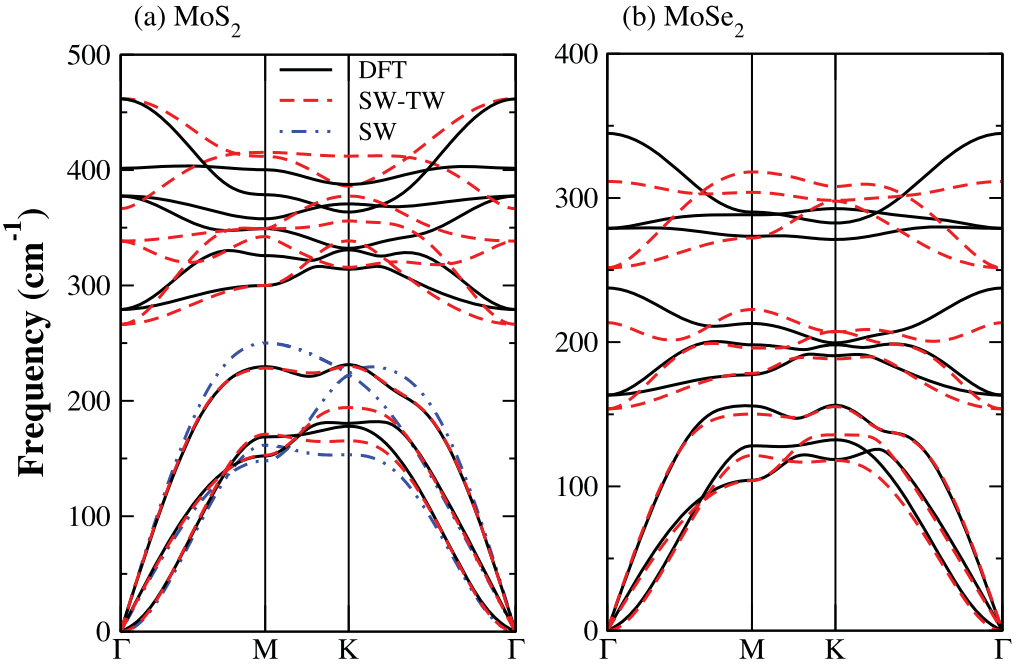

Figure 2. Phonon dispersions of monolayer (a) MoS_2 and (b) $MoSe_2$ along high-symmetry reciprocal space directions. The results of the first-principles calculations (DFT, black solid line), the SW-type IPP set developed in this work (SW-TW, red dashed line), and the SW-type IPP set presented in [27] (SW, blue dash-dot-dot line) are presented.

Table 2. Two-body SW parameters given in (2) and (3). This form is native to GULP.

	A	ρ	B	r_{min}	r_{max}
S–S	0.9641	0.9883	11.4454	0.00	3.82
Mo–S	5.0000	0.5985	16.8932	0.00	3.20
Mo–Mo	1.4867	0.9999	79.7857	0.00	4.27
Se–Se	1.8413	0.1000	20.0000	0.00	4.05
Mo–Se	30.0000	2.9998	30.0000	0.00	3.36
Mo–Mo	3.3741	1.0000	38.2674	0.00	4.55

process. This final sets produce highly consistent results with DFT in terms of lattice parameters, bond distances, and elastic constants (except C_{12} of $MoSe_2$) as given in table 1. Additionally, the force-field based vibrational properties of both single-layer MoS_2 and single-layer $MoSe_2$, especially longitudinal, transverse, and out-of-plane acoustic branches (LA, TA and ZA), have very good agreement with first-principles results. For these mode polarizations, we obtained a better fit (i.e shown as SW–TW in figure 2) to DFT results than a previously developed empirical potential [27] (i.e. shown as SW in figure 2). It should be noted that the SW-type IPP set is less successful in describing the vibrational properties is in the optical branches, especially at the higher end of the frequency scale. However, the effect of these phonons on lattice thermal conductivity is less important due to their very low phonon group velocities.

The developed IPP set governs the dynamics of atoms when coupled with the Newton's equations of motion as implemented in MD. The in-plane lattice thermal conductivities of MoS_2 and $MoSe_2$ are calculated from the classical description of atomic motion at equilibrium within fluctuation dissipation theory. Since the simulated structures contain no defects and edges, the main impediment in phonon conduction is the phonon–phonon scattering due to crystal anharmonicity. In this perspective, the calculated thermal conductivities of MoS_2 and $MoSe_2$ are given in figure 3(a) and (b). For the 200–500 K range, the κ of MoS_2 is found to decrease from 150 to 50 $Wm^{-1}K^{-1}$. In the case of $MoSe_2$, we find thermal conductivities almost half those for MoS_2 within the same temperature range. These values for MoS_2 and $MoSe_2$ are 5 to 50 times lower compared to single-layer hexagonal boron nitride [53] and graphene [56] evaluated with the same methods. When we compare our results with Boltzmann transport calculations [25, 26] we obtain good agreement at all temperatures. However, experimental measurements showed conductivities below 55 $Wm^{-1}K^{-1}$ at room temperature in MoS_2 [21–23] . There are possible reasons for this discrepancy between experimental and calculated results: one important feature of the classical description in our simulations is that every phonon mode is equally populated. This is consistent with material behavior above the Debye temperature (T_D). For the same reason, the temperature dependence of κ can be approximated by $1/T$ in figure 3. For materials simulated at temperatures much lower than (T_D) some scaling schemes may be needed to account for the differences in the populations between classical and quantum mechanics. When the temperature dependence of heat capacity is investigated it is seen that the majority of the phonons are populated for MoS_2 below 400 K, see the supplementary material, section 4. In the case of $MoSe_2$, this temperature is

Table 3. Three-body SW parameters given in (2) and (3). This form is native to GULP.

	K	θ_0	ρ_{12}	ρ_{13}	r_{12}^{max}	r_{13}^{max}	r_{23}^{max}
Mo–$S_{u,(d)}$–$S_{u,(d)}$	28.8462	82.5117	1.00	1.00	3.20	3.20	3.82
$S_{u,(d)}$–Mo–Mo	28.8462	82.5117	1.00	1.00	3.20	3.20	4.27
Mo–S_u–S_d	0.2357	80.8182	1.00	1.00	3.20	3.20	3.82
Mo–$Se_{u,(d)}$–$Se_{u,(d)}$	20.0000	81.5301	2.00	2.00	3.36	3.36	4.05
$Se_{u,(d)}$–Mo–Mo	20.0000	81.5301	2.00	2.00	3.36	3.36	4.55
Mo–Se_u–Se_d	13.1284	82.1288	2.00	2.00	3.36	3.36	4.05

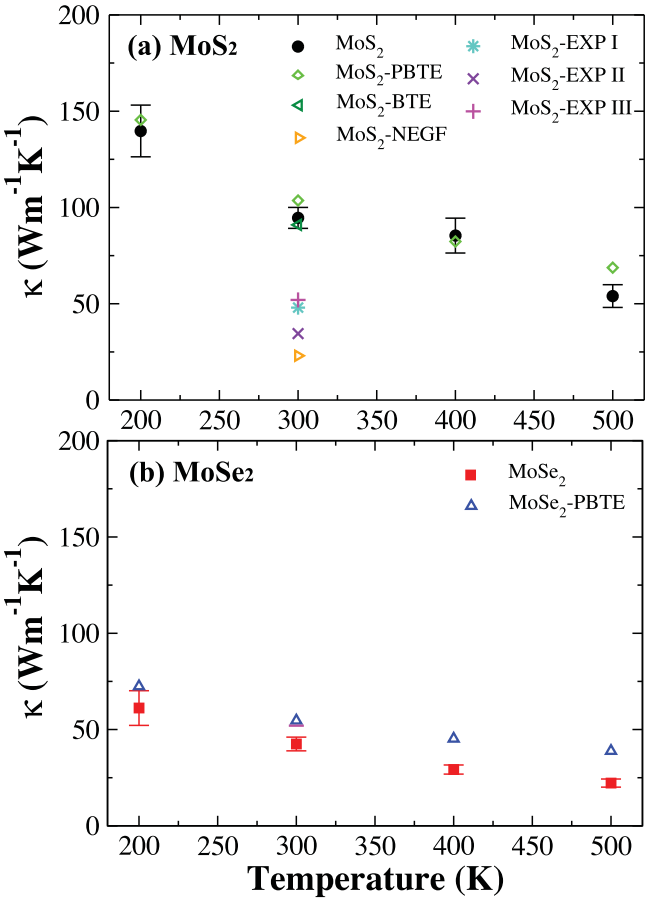

Figure 3. Calculated thermal conductivity values of MoS_2 and $MoSe_2$ as a function of temperature (black circles and red squares). The theoretical (PBTE [26], BTE [25], and NEGF [28]) and experimental (EXP I [20], EXP II [22], and EXP III [21]) values derived from the literature are also presented.

even lower, about 300 K, above which only few per cent change in heat capacity is observed. From these results it can be concluded that thermal conductivity predictions from MD do not require corrections above 300 K. Below this temperature our calculations are subject to larger discrepancies due to energy equipartition but since these materials reach the classical description around 300–400 K we do not expect serious errors. Another source of inconsistency could be related to the isotopes in the systems. In particular for molybdenum there are seven stable isotopes with natural abundances all below 25% [57]. With such a large spread in mass, the phonon scattering due to mass differences can be sizable and will be investigated in a future study. One final issue to consider is the effect of defects other than isotopes. In experimental measurements, it is impossible to completely eliminate imperfections such as point (vacancies, anti-sites, substitutionals, interstitials, surface contaminants, etc) and extended defects (grain boundaries, dislocations, edges, etc). These imperfections can significantly lower the thermal conductivity since they act as scatterers for phonons.

4. Conclusion

In summary, we presented a detailed investigation of the lattice thermal conductivity of two-dimensional crystals of MoS_2 and $MoSe_2$ using molecular level theories. For this purpose, using a particle swarm global optimization technique, we developed a unique Stillinger–Weber-type interaction potential parameter set that effectively represents the first-principles mechanical and vibrational properties of these structures. The optimized interatomic potential parameters reproduce the lattice thermal transport properties of these structures in quite good agreement with first-principles calculations. The differences between the calculated MoS_2 thermal conductivity and experimental results are possibly due to isotropic disorder and structural flaws that are inherent to measured structures.

Acknowledgments

C S acknowledges support from Anadolu University (BAP-1407F335, -1505F200) and the Turkish Academy of Sciences (TUBA-GEBIP). Computational resources were provided by TUBITAK ULAKBIM, High Performance and Grid Computing Center (TR-Grid e-Infrastructure). T C acknowledges support from NSF (Grant No. DMR 0844082) to the International Institute of Materials for Energy Conversion at Texas A&M University. Use of the Center for Nanoscale Materials, an Office of Science user facility, was supported by the US Department of Energy, Office of Science, Office of Basic Energy Sciences, under Contract No. DE-AC02–06CH11357.

References

[1] Radisavljevic B, Radenovic A, Brivio J, Giacometti V and Kis A 2011 *Nat. Nanotechnol.* **6** 147–50
[2] Lee C, Yan H, Brus L E, Heinz T F, Hone J and Ryu S 2010 *ACS Nano* **4** 2695–700
[3] Coleman J N *et al* 2011 *Science* **331** 568–71
[4] Elías A L *et al* 2013 *ACS Nano* **7** 5235–42
[5] Gutiérrez H R *et al* 2013 *Nano Lett.* **13** 3447–54
[6] Huang J K, Pu J, Hsu C L, Chiu M H, Juang Z Y, Chang Y H, Chang W H, Iwasa Y, Takenobu T and Li L J 2014 *ACS Nano* **8** 923–30
[7] Liu W, Kang J, Sarkar D, Khatami Y, Jena D and Banerjee K 2013 *Nano Lett.* **13** 1983–90
[8] Tongay S *et al* 2014 *Appl. Phys. Lett.* **104** 012101
[9] Kang J, Li J, Li S S, Xia J B and Wang L W 2013 *Nano Lett.* **13** 5485–90
[10] Chhowalla M, Shin H S, Eda G, Li L J, Loh K P and Zhang H 2013 *Nat. Chem.* **5** 263–75
[11] Wang H, Feng H and Li J 2014 *Small* **10** 2165
[12] Jariwala D, Sangwan V K, Lauhon L J, Marks T J and Hersam M C 2014 *ACS Nano* **8** 1102–20
[13] Larentis S, Fallahazad B and Tutuc E 2012 *Appl. Phy.Lett.* **101** 223104
[14] Dankert A, Langouche L, Kamalakar M V and Dash S P 2014 *ACS Nano* **8** 476–82
[15] Wang Q H, Kalantar-Zadeh K, Kis A, Coleman J N and Strano M S 2012 *Nat. Nanotechnol.* **7** 699–712
[16] Lee C, Hong J, Whangbo M H and Shim J H 2013 *Chem. Mater.* **25** 3745–52
[17] Huang W, Luo X, Gan C K, Quek S Y and Liang G 2014 *Phys. Chem. Chem. Phys.* **16** 10866–74
[18] Huang W, Da H and Liang G 2013 *J. Appl. Phys.* **113** 104304
[19] Fan D D, Liu H J, Cheng L, Jiang P H, Shi J and Tang X F 2014 *Appl. Phys. Lett.* **105** 133113
[20] Jo I, Pettes M T, Ou E, Wu W and Shi L 2014 *Appl. Phys. Lett.* **104** 201902
[21] Sahoo S, Gaur A P S, Ahmadi M, Guinel M J F and Katiyar R S 2013 *J. Phys. Chem.* C **117** 9042–7
[22] Yan R, Simpson J R, Bertolazzi S, Brivio J, Watson M, Wu X, Kis A, Luo T, Hight Walker A R and Xing H G 2014 *ACS Nano* **8** 986–93
[23] Peimyoo N, Shang J, Yang W, Wang Y, Cong C and Yu T 2014 *Nano Res.* **8** 1210
[24] Xu Y, Chen X, Gu B L and Duan W 2009 *Appl. Phys. Lett.* **95** 233116
[25] Li W, Carrete J and Mingo N 2013 *Appl. Phys. Lett.* **103** 253103
[26] Gu X and Yang R 2014 *Appl. Phys. Lett.* **105** 131903
[27] Jiang J W, Park H S and Rabczuk T 2013 *J. Appl. Phys.* **114** 064307
[28] Cai Y, Lan J, Zhang G and Zhang Y W 2014 *Phys. Rev.* B **89** 035438
[29] Kumar S and Schwingenschlögl U 2015 *Chem. Mater.* **27** 1278–84
[30] Zhou W-X and Chen K-Q 2015 *Sci. Rep.* **5** 15070EP
[31] Su J, Tang Liu Z, Ping Feng L and Li N 2015 *J. Alloys Compd.* **622** 777–82
[32] Wickramaratne D, Zahid F and Lake R K 2014 *J. Chem. Phys.* **140** 124710
[33] Stillinger F H and Weber T A 1985 *Phys. Rev.* B **31** 5262–71
[34] Jaramillo-Botero A, Naserifar S and Goddard W A 2014 *J. Chem. Theory Comput.* **10** 1426–39
[35] Larsson H R, van Duin A C T and Hartke B 2013 *J. Comput. Chem.* **34** 2178–89
[36] Kennedy J and Eberhart R C 1995 *Proc. IEEE Int. Conf. Neural Netw.* 4 1942
[37] Kennedy J, Eberhart R C and Shi Y 2001 *Swarm Intelligence* (New York: Academic)
[38] Clerc M and Kennedy J 2002 *IEEE Trans. Evol. Comput.* **6** 58–73
[39] Gale J D and Rohl A L 2003 *Molecular Simulation* **29** 291–341
[40] McQuarrie D A 2004 *Electronic Structure* (Cambridge: Cambridge University Press)
[41] Kresse G and Hafner J 1993 *Phys. Rev.* B **47** 558–61
[42] Kresse G and Furthmüller J 1996 *Phys. Rev.* B **54** 11169–86
[43] Kresse G and Furthmüller J 1996 *Comput. Mat. Sci* **6** 15–50
[44] Blöchl P E 1994 *Phys. Rev.* B **50** 17953–79
[45] Kresse G and Joubert D 1999 *Phys. Rev.* B **59** 1758–75
[46] Plimpton S 1995 *J. Comput. Phys.* **117** 1 – 19
[47] LAMMPS http://lammps.sandia.gov
[48] Green M S 1954 *J. Chem. Phys.* **22** 398–413
[49] Kubo R 1957 *J. Phys. Soc. Japan* **12** 570–86
[50] Martin R M 2000 *Statistical Mechanics* (Sausalito, CA: University Science)
[51] Allen M P and Tildesley D J 1987 *Computer Simulation of Liquids* (Oxford: Oxford University Press)
[52] Kinaci A, Haskins J B and Çağın T 2012 *J. Chem. Phys.* **137** 014106
[53] Sevik C, Kinaci A, Haskins J B and Çağın T 2012 *Phys. Rev.* B **86** 075403
[54] Haskins J B, Kinaci A, Sevik C and Çağın T 2014 *J. Chem. Phys.* **140** 244112
[55] Kinaci A, Haskins J B, Sevik C and Çağın T 2012 *Phys. Rev.* B **86** 115410
[56] Haskins J, Kinaci A, Sevik C, Sevinçli H, Cuniberti G and Çağın T 2011 *ACS Nano* **5** 3779–87
[57] Anbar A D 2004 *Rev. Mineral. Geochem.* **55** 429–54